ORIGINAL PAPER

CrossMark

Corrosion behavior of Ni-based coating containing spherical tungsten carbides in hydrochloric acid solution

Shan-shan Liu[1] · Hai-yan Chen[1,2] · Xuan Zhao[2] · Li Fan[2] · Xiao-ming Guo[1] · Yan-sheng Yin[2]

Abstract

A Ni-based alloy coating with 30 wt.% spherical tungsten carbide particles was prepared through plasma transferred arc welding on 42CrMo steel. The composition and microstructure of the coating were examined through X-ray diffraction and scanning electron microscopy with energy-dispersive spectrometry. The corrosion behaviors of the coating compared to the Ni coating without tungsten carbide particles and to the bare substrate in a 0.5 mol/L HCl solution were presented through polarization curves, electrochemical impedance spectroscopy (EIS) measurements and long-term immersion tests. The results demonstrated that the composite coating microstructure comprised Ni matrix, Ni-rich phase, tungsten carbide particles, W-rich phase and Cr-rich phase. The polarization curves and EIS measurements presented that a passivation film, which mainly included Ni, Cr, Fe and W oxides, was formed in the composite coating that protected the substrate from corrosion by HCl solution. In the immersion tests, a micro-galvanic reaction at the new-formed phases and Ni matrix interface caused severe pit corrosion and Ni matrix consumption. The debonding of Ni-rich and W-rich phases could be observed with the immersion time extension. The tungsten carbide particles and Cr-rich phase were still attached on the surface for up to 30 days.

1 Introduction

Recently, the rapid growth in energy demands has encouraged the exploitation of deep and acidic environments in the oil–gas fields. An acidic environment containing H^+ and Cl^- can induce severe corrosion and cause the destruction and waste of materials. Therefore, protective coatings exhibiting excellent mechanical properties and outstanding resistance are required by the oil–gas industry. Among the various corrosion resistance materials developed, the nickel-based alloys have outstanding

corrosion resistance properties, such as the reduction of oxidizing acids and resistance to pitting, stress corrosion cracking and crevice corrosion. The corresponding excellent corrosion resistance has led to the wide utilization of Ni-based coatings in various environments [1–3]. Scholl et al. [4] compared the corrosion resistance of three coatings, mainly comprising Co, Ni and Fe, with 10 vol.% tungsten carbides addition, confirming that (WC, Ni) had the best corrosion resistance in H_2SO_4 solution. However, the poor wear properties of Ni-based coating limited the application under the complex condition of wear and corrosion. To improve the poor wear resistance of Ni-based alloy coatings, the use of second phases such as SiC [5], WC [6] and Cr_3C_2 [7] particles to modify Ni-based coating in aggressive environments has attracted high research attention [8–10]. The effect of WC–Ni content on the structure and wear resistance of the coatings has been studied by Guo et al. [11]. The high-temperature resistance of laser-cladded NiCrBSi/WC–Ni composite coatings was also examined [12]. The addition of WC into these coatings

✉ Hai-yan Chen
hychen@shmtu.edu.cn

[1] School of Chemical and Environment Engineering, Shanghai Institute of Technology, Shanghai 201418, China

[2] College of Ocean Science and Engineering, Shanghai Maritime University, Shanghai 201306, China

was observed to highly increase the wear resistance at both room and high temperatures. Benea et al. [13] have shown that Ni/nano-WC composite exhibited a good wear resistance under both wet and dry conditions. The composite coatings containing these second phases (such as SiC, WC and Cr_3C_2) possess enhanced wear, corrosion and oxidation resistance, presenting dispersion hardening and self-lubrication compared to pure metals. Therefore, the composite coatings could effectively protect the metal substrate against aggressive environments during their operation [14]. Xu et al. [15] studied laser-cladded WC–Ni composite coatings with various contents of WC particles, discovering that the composite coating with 40 wt.% WC particles exhibited the best wear resistance among coatings with 0–80 wt.% WC.

The corrosion behavior was studied by Farahmand and Kovacevic [16] in a 3.5% NaCl solution, and Mohajeri et al. [17] focused on Ni/WC nano-composite in a sulfate solution. A passivation film was observed to form on the coating surface that protected the coating from corrosion by the corrosive solution. Particularly, a dense passivation film is associated with the microstructure and qualities of the surface. The hard phases in Ni-based alloy coatings increased the hardness and wear resistance, whereas the metallic binders ensured the corrosion resistance and integrity of the overall coating [18]. A coating with a denser fabricated layer and fewer cracks and pores has a greatly improved corrosion resistance [19, 20]. The development of advanced plasma transferred arc (PTA) welding technique has improved the quality of dense coatings with high adhesion strength and low porosity [21]. It is essential to study the corrosion behavior of layers processed through PTA technique, but previous studies mainly focused on the wear resistance of the coatings. Therefore, little information is presently available on the corrosion of Ni–WC coatings and particularly in a strong acidic environment [22].

This work aimed at the corrosion behavior investigation of Ni-based coatings containing spherical tungsten carbide particles in a 0.5 mol/L HCl solution, to contribute to more effective and extensive applications of Ni-based alloy coatings. The combined results of polarization curves, the electrochemical impedance spectroscopy (EIS) measurements and long-time immersion tests, as well as the corrosion behavior of Ni–WC composite coating, were studied. This paper provides insight into applications of Ni–WC coatings in HCl environment, while the relationship between corrosion behavior and chemical composition was clarified.

2 Experimental

2.1 Materials

The utilized Ni-based alloy and WC powders possessed a spherical morphology and a nominal particle size range of 45–145 μm, which are presented in Fig. 1. Unlike particles with other shapes, the spherical powder particles improve the powder fluidity and decrease the defects as well as the pores in the welding coating, while the spherical WC particles (Fig. 1b) exhibited an improved wettability with the bonding metal. The chemical composition of Ni-based alloy powders and WC particles is listed in Table 1. The self-fluxing Ni alloy powders were utilized as the binder and the tungsten carbide particles acted as reinforced particles, while the two powders were mixed with a weight ratio of 7:3. The composite coating was obtained through PTA welding (PTA-400E4-LM, Saint Gobain, France) on 42CrMo steel samples, identified herein as Ni–30WC. The working parameters were with the current of 130 A, voltage of 35 V, feed rate of 10 g/min, welding moving speed of 50 mm/min and vibration magnitude of 20 mm. The compositions and microstructures of the coatings were examined through X-ray diffraction (XRD) and scanning electron microscopy (SEM) with energy-dispersive spectrometry (EDS).
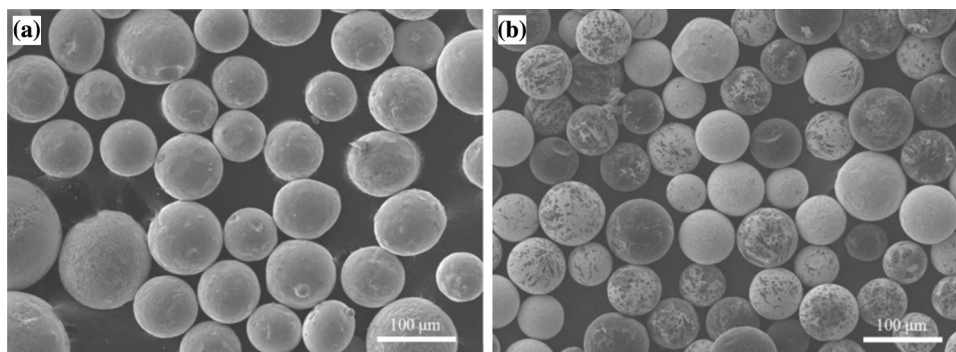

Fig. 1 SEM images of morphology of as-obtained Ni-based alloy (**a**) and WC powders (**b**)

Table 1 Chemical composition of Ni-based alloy powder and WC powder (wt.%)

Powder	Cr	Si	B	Fe	W	C	Ni
Ni-based alloy	15.85	4.45	3.11	12.3	–	0.46	Balance
WC	–		–	–	Balance	3.9–4.1	–

2.2 Electrochemical tests

The polarization curves and EIS results were obtained with an electrochemical system (Autolab PGSTAT302N, Metrohm AG), where the working cell was the standard three-electrode cell. The platinum network and saturated calomel electrode were the counter and reference electrodes, respectively. The sample was the working electrode. All tests were carried out in a 0.5 mol/L HCl electrolyte at room temperature. To obtain the polarization curves, the range of the scan potential was $-0.8\ V_{SCE}$ to $+0.8\ V_{SCE}$ (where V_{SCE} is the voltage with respect to the saturated calomel electrode) with a scan rate of 2 mV/s. Prior to measurements, the samples were soaked for 30 min in the electrolyte to ensure a steady-state condition.

EIS measurements were taken in static mode with 10 mV amplitude potential voltage in the frequency range of 10^{-2}–10^5 Hz. All measurements were taken twice to ensure good repeatability. Following, the corresponding parameters were calculated and simulated directly with the accompanying software of the unit. The parameters of each sample were observed to fluctuate within an acceptable tolerance.

2.3 Immersion tests

The immersion tests were carried out through the immersion of the samples in 0.5 mol/L HCl solution at a temperature of (25 ± 0.2) °C for a testing duration of 7, 14 and 30 days. Subsequently to test, the samples were ultrasonically cleaned with deionized water and dried. The corroded surfaces were observed through SEM and EDS. Furthermore, X-ray photoelectron spectroscopy (XPS) was utilized to analyze the composite coating surface after immersion for 7 days.

3 Results and discussion

3.1 Microstructure of Ni–30WC coating

XRD pattern of Ni–30WC coating is presented in Fig. 2. It could be observed that γ-Ni, γ-(Ni, Fe), Cr_7C_3, CrB, WC, W_2C and NiW_4C phases existed on the surface. SEM image of the cross section of the composite coating is shown in Fig. 3a. And the surface is shown in Fig. 3b–d.

EDS analysis (Table 2) of the coating surface demonstrated the existence of certain various morphologies, which could be distinguished to four parts and the tungsten carbide particles (labeled as points A, B, C, D and WC in Fig. 3d, respectively). The composition of point A was similar to the original Ni powders, and thus A can be inferred to Ni matrix. The microstructure of point B was dendritic, mainly consisting of Ni and Fe. Combined with XRD analysis results, point B was γ-Ni and γ-(Ni, Fe) phases, marked as Ni-rich phase. Similarly, point C was mainly composed of W, Ni and a low amount of C. Point C was NiW_4C or W_2C phase, marked as W-rich phase. The main element of point D was Cr. Point D was shaped like a spine-like microstructure [23], comprised of Cr_7C_3 or CrB phases and marked as Cr-rich phase. It was noted that a higher Fe amount existed in this phase compared to the original Ni-based alloy powder, which occurred due to the diffusion of Fe atoms from the steel substrate during PTA welding [6]. In PTA welding process, a low amount of 42CrMo substrate would melt and form a molten pool. In this pool, certain elements, such as Fe, Cr and C, could diffuse and combine with the powders. In this circumstance, both carbides and borides were easily formed. These newly formed reinforcing phases and compounds were evenly distributed in the plasma-induced surface coating, which contributed to the optimization of the wear and corrosion resistance of the coating. From the enlarged view of the interface in Fig. 3a, a thin white layer can be observed, which indicates that the composite coating has a
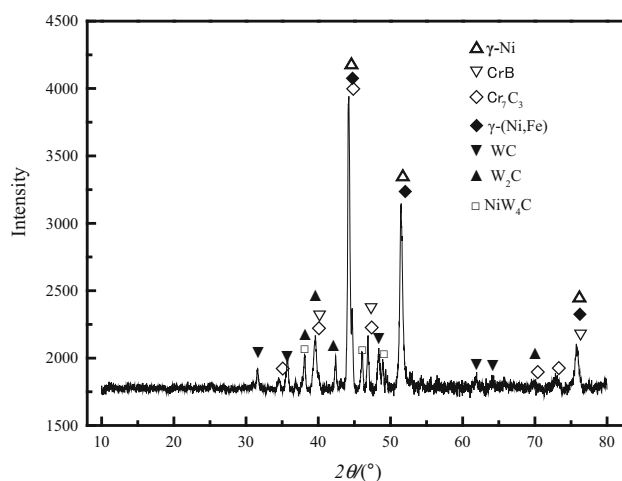
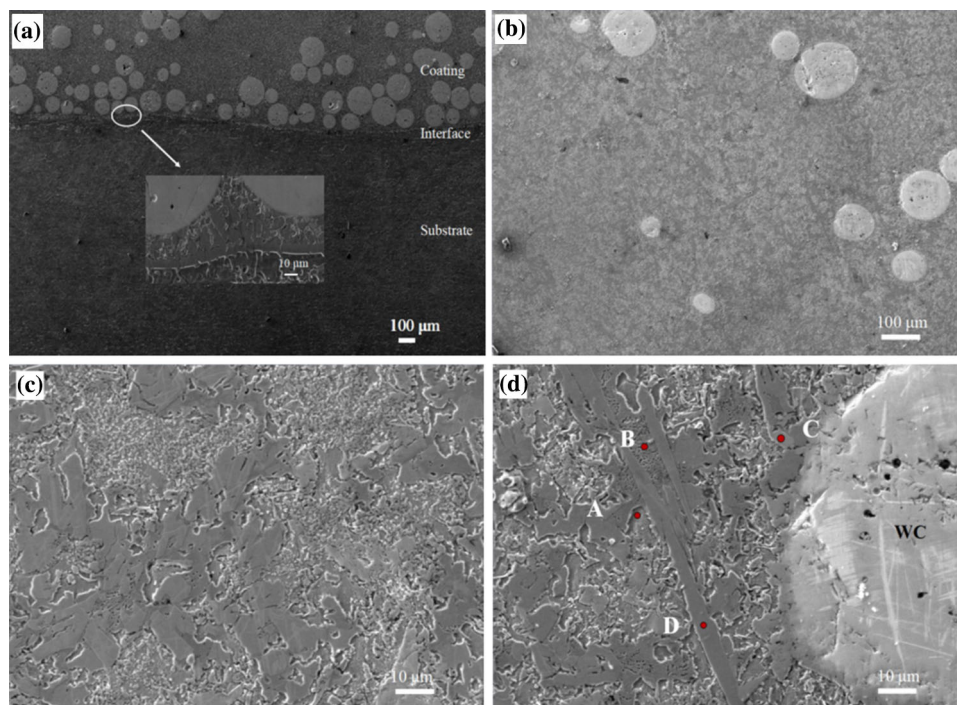**Fig. 2** XRD pattern of Ni–30WC composite coating

Fig. 3 SEM micrographs of Ni–30WC coating at locations of cross section (**a**), surface (**b**), higher-resolution images of surface (**c**) and surface area near tungsten carbide particle (**d**)

good metallic bonding with the substrate [24]. It can also be seen that most of the tungsten carbide particles have sunk to the bottom of the coating with few particles evident at the coating surface, which is owing to the higher melting point and larger density of WC than those of Ni-based alloy. Thus, the lower solidification rate and the lower melting point of Ni-based alloy allow WC particles to sink into the melt pool with insufficient convection currents within the melt pool to preclude the particle from sinking to the bottom [10, 18].

3.2 Electrochemical measurements

Figure 4 presents the polarization curves for the substrate, Ni and Ni–30WC coatings in 0.5 mol/L HCl solution. 42CrMo steel substrate exhibited an active anodic dissolution behavior, and no passivation region was observed. Furthermore, Ni and Ni–30WC had a noble direction compared to the substrate, where the substrate exhibited the

lowest self-corrosion potential value, confirming the strong effect of the bond coating on the potential. A typical passivation phenomenon could be observed in both Ni and Ni–30WC coatings. According to the passivation membrane adsorption theory [25], in the passivation region, the dissolved metal ions reacted with the oxygen atoms in the solution to produce a dense oxide film, which caused the current density not to exhibit apparent changes as the potential increased. The oxides, such as NiO, Fe_3O_4 and Cr_2O_3, protected the coating from further corrosion, which coincided well with the results reported by Zhang et al.

Table 2 EDS results of points in Fig. 3d labeled A–D (wt.%)

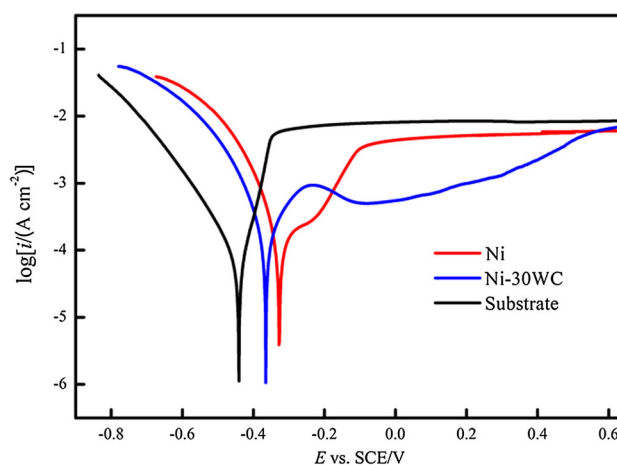| Point	Ni	W	Cr	Fe	C	Si
A	52.75	–	6.47	31.75	6.49	3.08
B	66.07	–	–	15.81	10.30	7.82
C	8.01	45.17	32.02	11.17	3.63	–
D	8.94	15.46	50.52	15.82	9.26	–

Fig. 4 Polarization curves of coating and substrate in 0.5 mol/L HCl solution

[26]. W-rich phase in the coating resulted from W diffusion from the tungsten carbide was dissolved in the solution and formed oxides on the surface, such as WO_3, which is beneficial to block the corrosion solution penetration. Besides the oxides, the increased passivation region in Ni–30WC coating might be associated with the dispersion of tungsten carbides on the surface and lower self-corrosion potential of tungsten carbide than that of Ni coating. The analysis data obtained from the polarization curves are presented in Table 3, in which the corrosion current I_{corr} value sequence was Ni–30WC coating < Ni-based alloy coating < substrate. Ni–30WC coating had a higher polarization resistance (R_p) value than Ni. Consequently, Ni–30WC coating exhibited a better corrosion resistance than Ni coating in HCl solution.

EIS results and the equivalent electrical circuits simulated to fit the impedance are shown in Fig. 5. For a better fitness, the capacitor was replaced with a constant phase element (CPE, Q), which was the cause of deviation from the ideal dielectric behavior, and the existing inhomogeneity and surface roughness [27]. In the equivalent electrical circuits (Fig. 5c, d), R_s represents the solution resistance, R_f represents the resistance caused by the ionic paths through the passivation layer, Q_f represents the capacitive behavior of the passivation film formed, R_{ct} represents the charge transfer resistance, Q_{dl} represents the resistance behavior of electric double layer, and L is the reactance. The Nyquist plots of the substrate in Fig. 5a presented a low-frequency inductive loop and a high-frequency capacitive loop, which were typical characteristics of iron dissolution in an acidic environment [28]. The low-frequency inductive loop was caused by the adsorption of corrosion products on the sample surface, while the high-frequency capacitive loop was associated with the charge transfer reaction [29]. The Nyquist plots of Ni and Ni–30WC coatings did not exhibit the low-frequency inductive arc, but exhibited a low-frequency capacitive arc. The arc semicircle diameter of Ni-30 coating was higher compared to Ni coating, which indicates an increase in corrosion consistence. Both a low- and a high-frequency capacitance arc were evident in Ni and Ni–30WC coatings. This indicated the formation of a passivation film on the coating surface, where the low-frequency capacitance was related to the passivation film and the high-frequency capacitance

was a response to the double-layer capacitance. The diameter of the arc semicircle of Ni-30 coating is greater than that of Ni coating, which indicates an increase in corrosion consistence. Table 4 presents $R(QR(QR))$ equivalent electrical circuit parameters of the Ni and Ni–30WC coatings. Table 5 presents $R(RQ)(LR)$ equivalent electrical circuit parameters of the substrate. In two tables, R_L denotes the inhibition of the effect of the adsorbed corrosion products on the electrode process, Y_0 is a constant related to potential, and n is a parameter of no unit, which is account for the deviation from the ideal dielectric behavior. Concerning to the listed data, the resistance values of Ni and Ni–30WC were significantly higher compared to those of 42CrMo substrate. The value of R_f (1881 Ω cm^2) of Ni–30WC coating was approximately 2.3 times than that (780 Ω cm^2) of Ni coating, which indicated that Ni–30WC and Ni coatings could protect the substrate from corrosion and Ni–30WC coating serves as a more effective barrier layer to corrosion.

From the Bode plots of Ni and Ni–30WC coatings in Fig. 5b, two time constants were observed to be superimposed together and appeared as a widened capacitive loop. The Bode plots could be divided into three parts: (1) The first part was a high-frequency region (10^3–10^5 Hz), where the impedance was dominated by the electrolyte resistance; (2) the second part was an intermediate-frequency region (1–10^3 Hz), where the phase angle reached its maximum θ_{max}, approaching $-90°$, which was the characteristic capacitive behavior; (3) the third part was a low-frequency region (10^{-2}–1 Hz), where the value of |Z| represented the corrosion reaction impedance. A higher value of |Z| for Ni–30WC coating in the low-frequency region can be observed in Fig. 5b, indicating that the passivation films on Ni–30WC coating offered a high corrosion resistance. The results were consistent with the Nyquist plots results.

3.3 Surface analyses after corrosion

Ni–30WC coating surface was corroded through immersion in a 0.5 mol/L HCl solution for 7, 14 and 30 days. SEM images of the coating surfaces are presented in Fig. 6. Subsequently to immersion for 7 days (Fig. 6a, b), the tungsten carbide particles on the surface appeared unaffected by the solution, even though Ni matrix sustained

Table 3 Polarization curve results for corrosion potential (E_{corr}), I_{corr}, R_p and Tafel slopes (β_a and β_c)

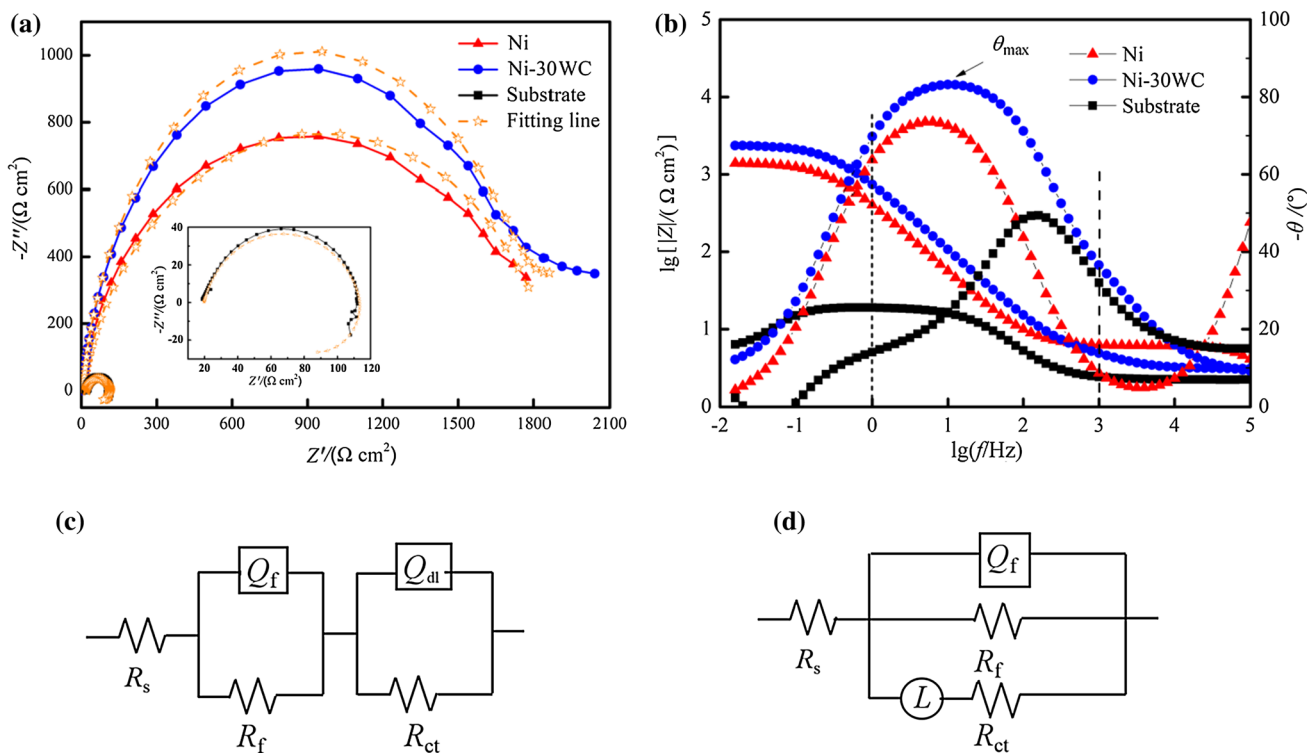| Sample	E_{corr}/V	I_{corr}/(μA cm^{-2})	R_p/Ω	β_a/(mV dec^{-1})	β_c/(mV dec^{-1})
Substrate	− 448.90	365.59	71.70	213.81	84.09
Ni	− 346.18	24.55	856.01	79.43	123.80
Ni–30WC	− 367.61	9.097	2458.50	107.98	98.45

Fig. 5 Nyquist plots (a), Bode plots (b), and equivalent electrical circuits of EIS for Ni and Ni–30WC coatings (c) and substrate (d). f Angular frequency; θ phase angle; θ_{max} phase angle close to $-90°$; Z impedance of system; Z' real part of impedance; Z'' imaginary part of impedance

Table 4 EIS fitting results of Ni and Ni–30WC coatings in 0.5 mol/L HCl solution

Sample	$R_s/(\Omega \ cm^2)$	Q_f		$R_f/(\Omega \ cm^2)$	Q_{dl}		$R_{ct}/(\Omega \ cm^2)$
		$Y_0/(\Omega^{-1} \ cm^{-2} \ s^n)$	n		$Y_0/(\Omega^{-1} \ cm^{-2} \ s^n)$	n	
Ni–30WC	2.31	2.85×10^{-4}	0.94	1881	7.42×10^{-3}	0.8029	7.07
Ni	2.21	2.84×10^{-4}	0.91	780	1.797×10^{-2}	0.42	4.17

Table 5 EIS fitting results of substrate in 0.5 mol/L HCl solution

Sample	$R_s/(\Omega \ cm^2)$	Q_f		$R_{ct}/(\Omega \ cm^2)$	$L/(H \ cm^{-2})$	$R_L/(\Omega \ cm^2)$
		$Y_0/(\Omega^{-1} \ cm^{-2} \ s^n)$	n			
Substrate	1.98	3.92×10^{-5}	0.83	94.76	134.8	73.49

severe dissolution. The composition analysis of the surface was obtained through EDS on the points labeled A1, B1, C1 and D1 in Fig. 6a, while the results are given in Table 6. After immersion for 14 days (Fig. 6c, d), certain pits appeared at A1 and C1 interface, D1 and A1 interface, as well as A1 and B1 interface. From a basic analysis of EDS results, the points labeled A1, B1, C1 and D1 in Fig. 6b could be regarded as Ni matrix, Ni-rich phase, W-rich phase and Cr-rich phase, respectively.

Subsequently to immersion for 14 days, most W-rich and Cr-rich phases remained on the corroded surface, while Ni-rich phase was dissolved. When the immersion time reached 30 days (Fig. 6c, d), only Cr-rich phase and the tungsten carbide particles remained on the corroded surface, whereas W-rich phase areas, having lost Ni matrix support, were detached from the surface. From the observed variation of the corroded surface with different immersion durations, it was clear that the second phase
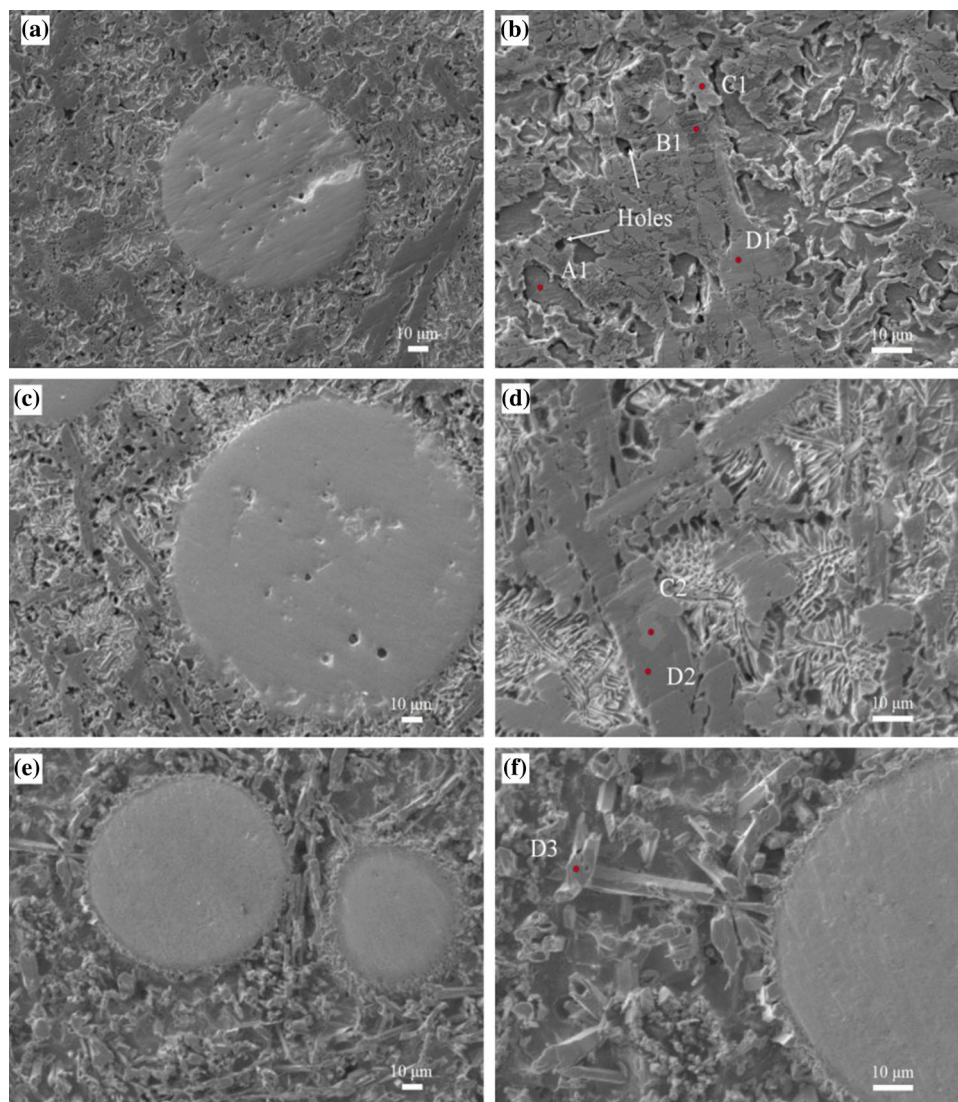
Fig. 6 SEM images of corroded surface of Ni–30WC coating immersed in 0.5 mol/L HCl solution for 7 (**a**, **b**), 14 (**c**, **d**) and 30 days (**e**, **f**)

Table 6 EDS results of coating surface at points A1–D1 in Fig. 6b, C2 and D2 in Fig. 6d, and D3 in Fig. 6f (wt.%)

Point	Ni	W	Cr	Fe	C	O	Si
A1	85.56	–	–	6.51	3.21	9.01	6.71
B1	62.55	–	6.83	15.94	0.21	3.02	11.45
C1	5.71	58.60	22.01	11.80	1.88	–	–
D1	9.23	8.39	69.64	12.32	0.42	–	–
C2	24.83	53.49	15.23	5.49	0.27	0.69	
D2	12.97	15.71	50.65	20.23	0.44	–	–
D3	8.13	12.14	54.73	24.57	0.43	–	–

acted as a physical skeleton to protect Ni matrix from preferential corrosive attack. Certain regions joining the phases would still be depleted; however, the potential for micro-galvanic activity at the surface increased the heterogeneity of the local attack [16]. The heterogeneity of the physical or chemical can cause the serious influence on pitting corrosion. The metal with lower potential prefers location for metal dissolution or the pit initiation [30]. Initially, Ni matrix and Ni-rich phase were attacked by HCl, while Cr-rich and W-rich phases possessed improved corrosion resistance. The corrosion began at the interfaces among these phases, while the pit formation mainly occurred owing to the resulting micro-galvanic activity. This galvanic effect occurs at areas of larger potential, when the two areas had different potentials [31, 32]. Cr- or W-rich regions acted as cathodic sites, Ni matrix acted as a cathodic site and the micro-galvanic reaction consequently consumed Ni matrix. The debonding of Ni-rich phase could be observed first, followed by W-rich debonding. The acidic solution penetrated the new contact surface, and the

migration of H^+ and Cl^- to the corroded surface through the holes or pits caused a further attack to the uncorroded surface [33].

After immersion testing in HCl solution, WC particles and Cr-rich phase remained virtually unaffected. The corrosion behavior of the surface presented a close relationship to Ni binder, whereas the main elements of the original Ni powders were Ni, Cr and Fe. An XPS analysis was obtained of Ni–30WC coating after immersion for 7 days and is presented in Fig. 7. Ni $2p_{3/2}$ spectrum consisted of four peaks located at 856.73, 874.33, 862.35 and 880.82 eV, corresponding to the presence of Ni, NiO, Ni_2O_3 and $Ni(OH)_3$, respectively [34, 35]. Cr $2p_{3/2}$ spectrum consisted of three peaks corresponding to the three doublet states of Cr^0, Cr^{3+} and Cr^{6+} states, respectively, as well as of the peaks located at 574.38 eV(Cr), 576.59 eV (Cr_2O_3), 578.3 eV (CrO_3), and 586.7 eV ($Cr(OH)_3$). Fe $2p_{3/2}$ spectrum could be divided into four peaks, which were allocated to Fe (709.4 eV), Fe_3O_4 (723.5 eV), Fe_2O_3 (711.4 eV), and $FeCr_2O_4$ (725 eV). In W $4f$ spectra

(Fig. 7), the peak of WO_3 (37.4 and 35.2 eV) can be detected in the coating surface, which is consistent with the results of some researchers [26, 36].

Through the combination of these XPS results with the results from the electrochemical experiments (Fig. 4 and Table 3), the corrosion behavior of Ni–30WC composite coating could be clearly observed. The passivation phenomenon appearing during HCl corrosion induced a decreased I_{corr} value and an increased impedance, where the passivation film occurred mainly due to the formation of Ni, Cr, Fe and W oxides. Cr of the coating could also form a new hard phase (Cr_7C_3), where a newly formed second phase could significantly increase the hardness of the overlay and consequently improve the wear resistance of the composite coating [37, 38]. Adversely, the newly formed phases and WC particles could exacerbate the occurrence of micro-galvanic cells, which occurred due to the inhomogeneous distribution of phases in the overlay and the potential difference from the binder, causing severe pit corrosion. The acidic corrosion penetrated the coating
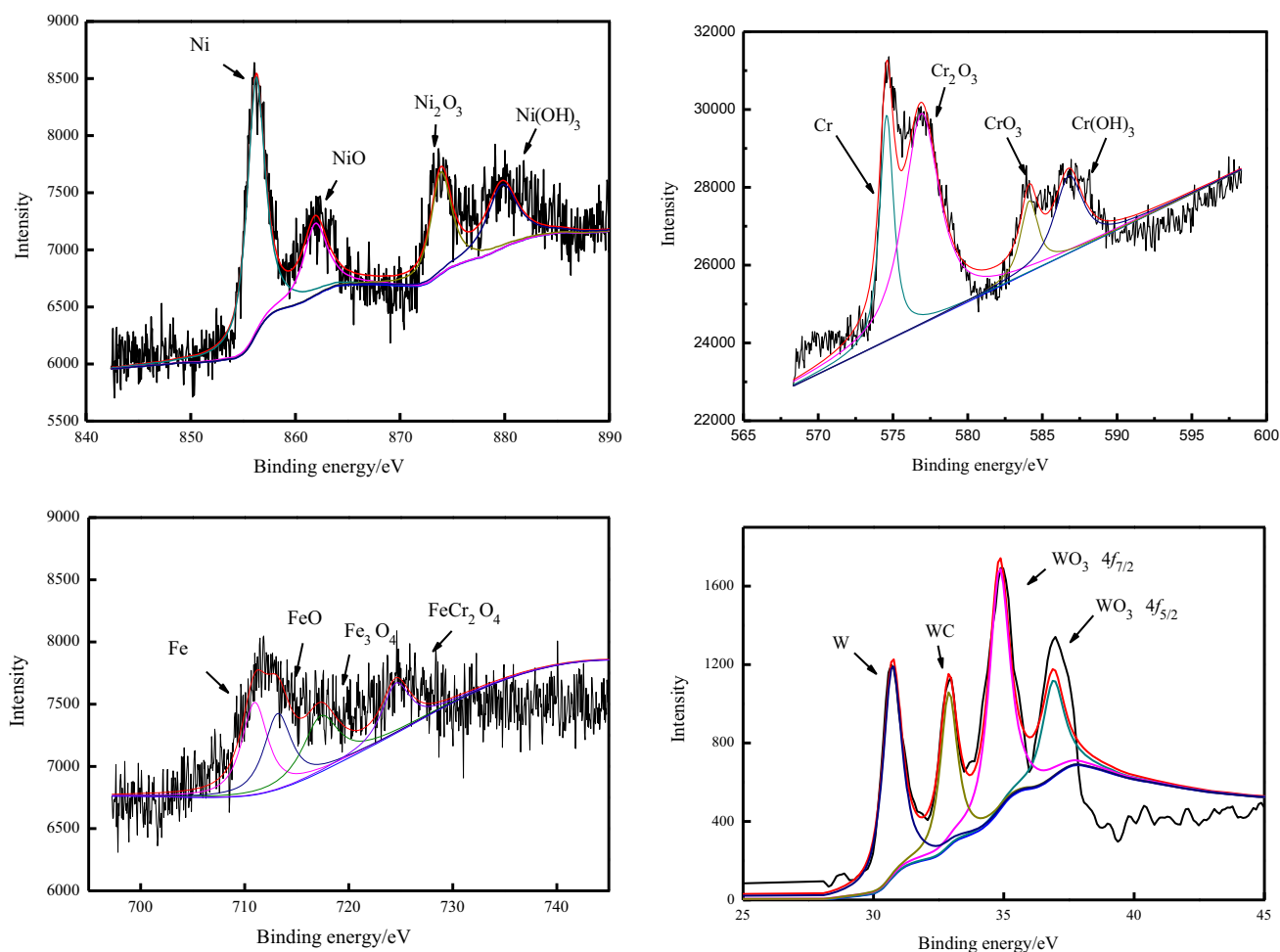

Fig. 7 Detailed XPS spectra of Ni $2p_{3/2}$, Cr $2p_{3/2}$, Fe $2p_{3/2}$ and W $4f$ of coating surface on Ni–30WC in 0.5 mol/L HCl solution for 7 days

interior through the pits or new contact surfaces, provided by the debonding of the second phases, which finally caused the further attack of the coating.

4 Conclusions

1. The microstructure of the composite coating can be considered as Ni matrix, Ni-rich phase containing γ-Ni and γ-(Ni, Fe), Cr-rich phase containing Cr_7C_3 and CrB, as well as W-rich phase containing NiW_4C. The composite coating had a good bonding with the substrate. Most tungsten carbides sunk to the bottom of the coating.

2. The samples coated with Ni–30WC and Ni exhibited a better corrosion resistance than the bare substrate. The corrosion resistance of Ni–30WC coating was superior to that of Ni coating, due to a protective film consisted of Ni, Cr, Fe and W oxides.

3. Micro-galvanic activity formed in the interface between new-formed phases and Ni matrix causing serious pit corrosion and consumption of Ni matrix. The acidic corrosion infiltrated into the new contact surfaces was provided by debonding of the second phases and pits, causing the further attack of the coating.

References

[1] Q.Y. Wang, X.Z. Wang, H. Luo, J.L. Luo, Surf. Coat. Technol. 291 (2016) 250–257.
[2] P. Crook, Mater. Corros. 56 (2005) 606–610.
[3] S.E. Ziemniak, M. Hanson, Corros. Sci. 45 (2003) 1595–1618.
[4] H. Scholl, B. Hofman, A. Rauscher, Electrochim. Acta 37 (1992) 447–452.
[5] M.R. Vaezi, S.K. Sadrnezhaad, L. Nikzad, Colloid. Surface A 315 (2008) 176–182.
[6] E. Fernández, M. Cadenas, R. González, C. Navas, R. Fernández, J. de Damborenea, Wear 259 (2005) 870–875.
[7] S.P. Li, D. Feng, H.L. Luo, H.E. Zhang, X. Cao, J. Iron Steel Res. Int. 13 (2006) No. 6, 37–40, 59.
[8] A. Conde, F. Zubiri, Y.J. de Damborenea, Mater. Sci. Eng. A 334 (2002) 233–238.
[9] J. Rodríguez, A. Martín, R. Fernández, J.E. Fernández, Wear 255 (2003) 950–955.
[10] P. Wu, H.M. Du, X.L. Chen, Z.Q. Li, H.L. Bai, E.Y. Jiang, Wear 257 (2004) 142–147.
[11] C. Guo, J.M. Chen, J.S. Zhou, J.R. Zhao, L.Q. Wang, Y.J. Yu, H.D. Zhou, Surf. Coat. Technol. 206 (2012) 2064–2071.
[12] C. Guo, J.M. Zhou, J.S. Chen, J.R. Zhao, Y.J. Yu, H.D. Zhou, Wear 270 (2011) 492–498.
[13] L. Benea, S. Başa, E. Dănăilă, N. Caron, O. Raquet, P. Ponthiaux, J. Celis, Mater. Des. 65 (2015) 550–558.
[14] S.T. Aruna, V.K. William, G.K.S. Rajam, J. Alloy. Compd. 468 (2009) 546–552.
[15] J.S. Xu, X.C. Zhang, F.Z. Xuan, Z.D. Wang, S.T. Tu, J. Mater. Eng. Perform. 21 (2012) 1904–1911.
[16] P. Farahmand, R. Kovacevic, Surf. Coat. Technol. 276 (2015) 121–135.
[17] S. Mohajeri, A. Dolati, S. Rezagholibeiki, Mater. Chem. Phys. 129 (2011) 746–750.
[18] M.J. Tobar, C. Álvarez, J.M. Amado, G. Rodríguez, A. Yáñez, Surf. Coat. Technol. 200 (2006) 6313–6317.
[19] S.S. Zhou, X.Y. Zeng, Q.W. Hu, Y.J. Huang, Appl. Surf. Sci. 255 (2008) 1646–1653.
[20] X.C. Zhang, B.S. Xu, Y.X. Wu, F.Z. Xuan, S.T. Tu, Appl. Surf. Sci. 254 (2008) 3879–3889.
[21] Z.Q. Zhang, H.D. Wang, B.S. Xu, G.S. Zhang, Surf. Coat. Technol. 261 (2015) 60–68.
[22] J.E. Cho, S.Y. Hwang, K.Y. Kim, Surf. Coat. Technol. 200 (2006) 2653–2662.
[23] A. Zikin, I. Hussainova, C. Katsich, E. Badish, C. Tomastilk, Surf. Coat. Technol. 206 (2012) 4270–4278.
[24] Z.Y. Huang, Q.Y. Hou, P. Wang, Surf. Coat. Technol. 202 (2008) 2993–2999.
[25] L.F. Liu, C.Y. Chao, D.D. Macdonald, J. Electrochem. Soc. 128 (1981) 1194–1198.
[26] Q.K. Zhang, N. Lin, Y.H. He, Int. J. Refract. Met. Hard Met. 38 (2013) 15–25.
[27] D. Bartkowski, A. Młynarczak, A. Piasecki, B. Dudziak, M. Gościański, A. Bartkowska, Opt. Laser Technol. 68 (2015) 191–201.
[28] H.B. Fan, W. Zhang, G.Y. Wang, P.K. Liaw, J. Shen, Metall. Mater. Tran. A 42 (2011) 1524–1533.
[29] A. Bartkowska, A. Pertek, M. Popławski, D. Bartkowski, D. Przestacki, A. Mikaszewski, Opt. Laser Technol. 72 (2015) 116–124.
[30] Y.T. Zhao, C.H. Jiang, Z. Xu, F. Cai, Z.Q. Zhang, P. Fu, Mater. Des. 85 (2015) 39–46.
[31] S. Matthew, B. James, M. Hyland, Corros. Sci. 51 (2009) 1172–1180.
[32] A. Lekatou, E. Regoutas, A.E. Karantzalis, Corros. Sci. 20 (2008) 3389–3400.
[33] J.H. Chang, J.M Chou, R.I. Hsieh, J.L. Lee, Corros. Sci. 51 (2009) 987–996.
[34] Y. Gao, B.H. Luo, K.J. He, W.W. Zhang, Z.H. Baia, Ceram. Int. 44 (2018) 2030–2041.
[35] L. Zhang, D.D. Macdonalda, Electrochim. Acta 43 (1998) 2661–2671.
[36] S. Oswald, W. Brückner, Surf. Interface Anal. 36 (2004) 17–22.
[37] N. Elkhoshkhany, A. Hafnway, A. Khaled, J. Alloy. Compd. 695 (2017) 1505–1514.
[38] R. Sundaramoorthy, S.X. Tong, D. Parekh, C. Subramanian, Wear 376-377 (2017) 1720–1727.